PNAS RESEARCH ARTICLE | CELL BIOLOGY OPEN ACCESS

Pleiotropic role of TRAF7 in skull-base meningiomas and congenital heart disease

Ketu Mishra-Gorur[a,1], Tanyeri Barak[a], Leon D. Kaulen[a], Octavian Henegariu[a], Sheng Chih Jin[b], Stephanie Marie Aguilera[a], Ezgi Yalbir[a], Gizem Goles[a], Sayoko Nishimura[a], Danielle Miyagishima[a], Lydia Djenoune[c], Selin Altinok[a], Devendra K. Rai[a], Stephen Viviano[d], Andrew Prendergast[e], Cynthia Zerillo[a], Kent Ozcan[a], Burcin Baran[a], Leman Sencar[a], Nukte Goc[a], Yanki Yarman[a], A. Gulhan Ercan-Sencicek[a], Kaya Bilguvar[b], Richard P. Lifton[b,f], Jennifer Moliterno[a,g], Angeliki Louvi[a,h], Shiaulou Yuan[c], Engin Deniz[d], Martina Brueckner[d], and Murat Gunel[a,b,g,h,1]

Edited by Randall T. Peterson, The University of Utah, Salt Lake City, Utah; received September 2, 2022; accepted February 27, 2023 by Editorial Board Member Jeremy Nathans

While somatic variants of *TRAF7* (Tumor necrosis factor receptor-associated factor 7) underlie anterior skull-base meningiomas, here we report the inherited mutations of *TRAF7* that cause congenital heart defects. We show that TRAF7 mutants operate in a dominant manner, inhibiting protein function via heterodimerization with wild-type protein. Further, the shared genetics of the two disparate pathologies can be traced to the common origin of forebrain meninges and cardiac outflow tract from the *TRAF7*-expressing neural crest. Somatic and inherited mutations disrupt TRAF7–IFT57 interactions leading to cilia degradation. *TRAF7*-mutant meningioma primary cultures lack cilia, and TRAF7 knockdown causes cardiac, craniofacial, and ciliary defects in *Xenopus* and zebrafish, suggesting a mechanistic convergence for *TRAF7*-driven meningiomas and developmental heart defects.

TRAF7 | meningioma | cilia | congenital heart defect

TRAF7 is the most recently identified member of the TRAF family, which is comprised of modular adapter-type proteins that mediate the assembly of cytoplasmic signal transducers and regulators downstream of receptor complexes (1). TRAF7 contains N-terminal RING and zinc finger domains characteristic of TRAF proteins, but lacks the conserved C-terminal TRAF domain, and harbors instead seven WD40 repeats (2, 3). It is an E3 ubiquitin ligase that physically interacts with and potentiates MEKK3 signaling (3, 4), ubiquitinates NEMO and p65, integral parts of the NF-kB pathway for degradation (2, 4, 5), and serves as a scaffold for the NF-kB and Jun/AP1 pathways critical for cell proliferation and survival (1).

TRAF7 dysfunction has been implicated in human disease. Using next-generation sequencing technologies, we and others discovered somatic *TRAF7* driver mutations in meningiomas, the most common primary intracranial tumor (6), underlying nearly one-fourth of all and the entirety of the secretory subtype (7, 8). TRAF7 somatic mutations are necessary but not sufficient to drive meningioma formation as they co-occur either with a recurrent K409Q somatic mutation in KLF4 or an activating mutation in one of the molecules of the PI3K pathway (7). KLF4 is one of the four transcription factors sufficient to induce pluripotent cells from terminally differentiated ones (9). Similarly, somatic *TRAF7* aberrations have also been implicated as possible pathogenic drivers in mesothelioma (10), adenomatoid tumors (11), and intraneural perineuriomas (12).

On the contrary, d*e novo* germline missense TRAF7 variants have been reported in individuals with developmental delay, congenital heart disease (CHD), limb anomalies, and dysmorphic features (13). The phenotypic and pathological diversity associated with TRAF7 dysfunction is potentially explained by underlying commonalities in the embryologic origin of the affected organs: Meningiomas harboring TRAF7 mutations localize anterior to the foramen magnum in the skull base, a region of the brain enclosed by meninges derived from the neural crest (14), an embryonic migratory cell population that also generates the craniofacial skeleton and further contributes to the septation of the cardiac outflow tract and ventricles (15). This common embryologic origin emphasizes a potential overlap in the pathobiology of meningioma harboring somatic mutations in *TRAF7* and neural crest cell pathologies including congenital cardiac and craniofacial defects.

Here, we examine the functional consequences of meningioma-associated somatic (i.e., heterozygous) mutations and report inherited mutations in *TRAF7* in 3 unrelated individuals with CHD. We establish that mutant forms of TRAF7 can heterodimerize with and disrupt the function of the wild-type (WT) protein, leading to loss of MEKK3 binding and reduction of JNK activation. We further demonstrate that both the somatic and the inherited mutations disrupt TRAF7–IFT57 interactions and thereby, intraflagellar

Significance

The genetic basis for the increased risk of cancer with congenital heart disease (CHD) is largely unclear. Our study is significant because it identifies TRAF7 (Tumor necrosis factor receptor-associated factor 7) mutations in both, brain tumors (meningiomas) and CHD. While somatic mutations in TRAF7 underlie anterior skull-base meningiomas, here we report the inherited mutations of TRAF7 that cause CHD and show that the shared genetics of the two disparate pathologies can be traced to the common developmental origin of the two tissues from the neural crest. We demonstrate that these mutations act as dominant negative by dimerizing with wild-type TRAF7 and disrupting its function and ascribe a unique role for TRAF7 in ciliogenesis and intraflagellar transport.

Author contributions: K.M.-G. designed research; K.M.-G., T.B., L.D.K., O.H., S.C.J., S.M.A., E.Y., G.G., S.N., D.M., L.D., S.A., D.K.R., S.V., A.P., C.Z., K.O., B.B., L.S., N.G., Y.Y., A.G.E.-S., S.Y., and E.D. performed research; K.M.-G., T.B., S.C.J., D.M., L.D., S.V., K.B., R.P.L., S.Y., E.D., M.B., and M.G. analyzed data; J.M. contributed meningioma samples; M.B. contributed human patient data; M.G. led the research; and K.M.-G., A.L., and E.D. wrote the paper.

The authors declare no competing interest.

This article is a PNAS Direct Submission. R.T.P. is a guest editor invited by the Editorial Board.

[1]To whom correspondence may be addressed. Email: ketu.mishra@yale.edu or murat.gunel@yale.edu.

This article contains supporting information online at https://www.pnas.org/lookup/suppl/doi:10.1073/pnas.2214997120/-/DCSupplemental.

Published April 12, 2023.

transport and cilia maintenance, and that *TRAF7* knockdown causes cardiac, craniofacial, and ciliary defects in *Xenopus tropicalis* and zebrafish.

Results

***TRAF7* Mutations Are Predicted to Alter Protein Structure.** We have previously demonstrated that meningiomas harboring somatic mutations in *TRAF7* localize laterally along the skull base and mostly anterior to the coronal suture along the convexities (7); the vast majority (93%) of these variants map to the C-terminal WD40 domains (Fig. 1*A* and *SI Appendix*, Fig. S1*A*). Homology protein modeling (7) indicated that TRAF7 contains a putative ligand-binding or protein interaction β-propeller domain with hydrophobic loops (Fig. 1 *B* and *C*), which resembles the ligand-binding site of the Groucho-TLE WD40 domain (PDB: 2CE9) (*SI Appendix*, Fig S1 *B* and *C*). The meningioma-associated mutations (Fig. 1*A*) affect amino acids within the hydrophobic loops between the β-blades in the β-propeller and would be expected to disrupt the hydrophobic interaction network formed by residues P398, W400, I441, and V661. Mutations affecting residues N520 and G536, which are most frequently altered to a serine in meningiomas, are predicted to impact WD40 domain structure, with N520S forming hydrogen bonds only with one, instead of two, β-strand of the preceding blade of the β-propeller, thereby introducing conformational flexibility (Fig. 1*D*). Mutations in tyrosine residues Y563, Y603, and Y621, which would be predicted to engage in extensive interactions with W522, T601, A604, and A648 to form a hydrophobic patch with W400, are predicted to disrupt this region in the ligand-binding surface and, as a result, introduce significant local structural changes (Fig. 1*E*). Analogous changes are expected when residue W400 is mutated (Fig. 1*F*). Overall, meningioma-associated missense mutations are predicted either to disrupt the interactions of TRAF7 with other proteins, or to alter the structure of the WD40 domains.

WT and Mutant TRAF7 Heterodimerize and Disrupt Protein–Protein Interactions. To validate the predictions of homology protein modeling experimentally, we examined the functionality of four randomly selected meningioma-associated missense mutations (C388Y, G536S, K615E, and R653Q) (Fig. 1*A*). We found that WT and mutant TRAF7 can, indeed, form

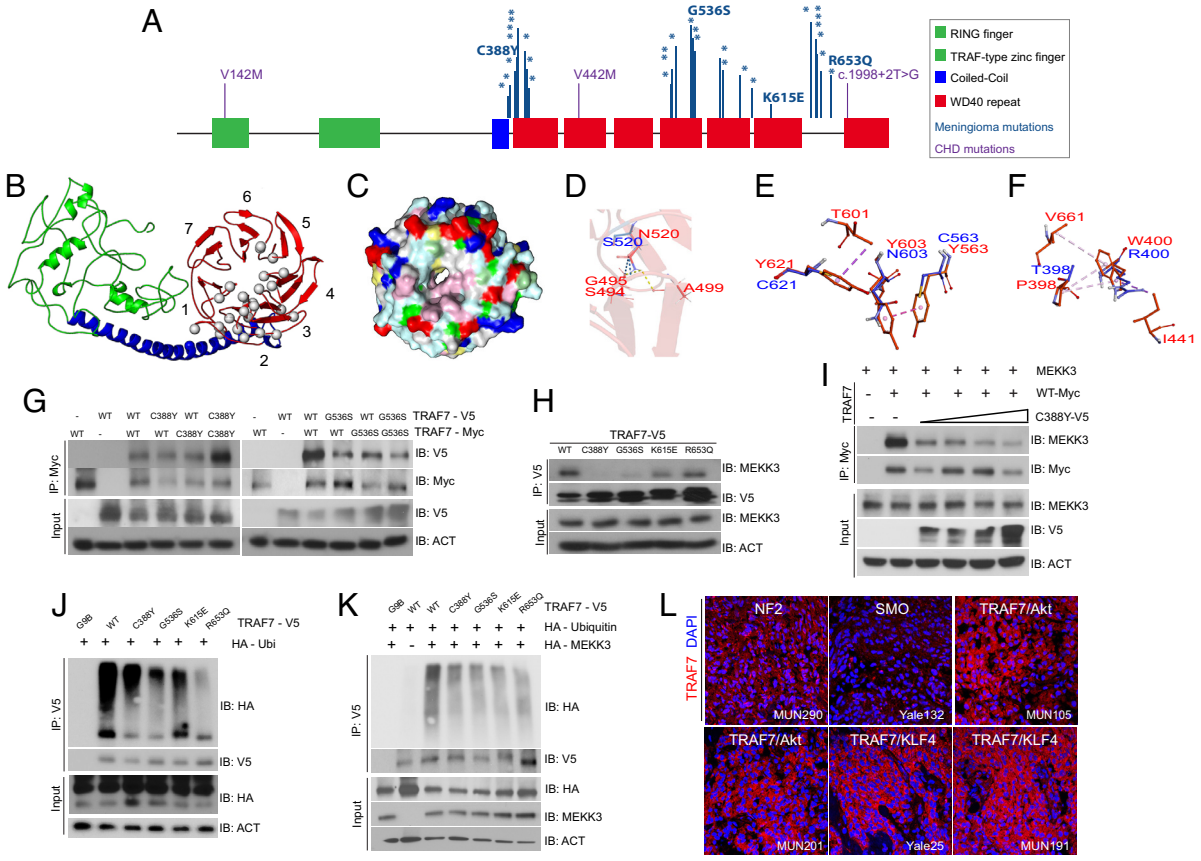

Fig. 1. TRAF7 mutations disrupt protein structure and interactions. (*A*) Protein structure of TRAF7; developmental variants V142M, V442M, and c.1998+2T>G and the locations of previously reported (16) meningioma-associated mutations (asterisks; 93% map to the WD40 domains), including those analyzed in this study. (*B*) Predicted structure of TRAF7. The RING finger (green), coiled-coil (blue), and putative 7-WD40-repeat-containing putative ligand-binding (red) domains are indicated. The mutations (gray circles) are primarily localized to one face of the latter. (*C*) Representation of the WD40-domain molecular surface, exhibiting a hydrophobic patch (pink, reflecting concentration of white [small hydrophobic] and magenta [aromatic] residues) surrounding the pore of the β-propeller surface. Yellow: cysteine; pale green: proline; green: glycine; cyan: polar; blue: positively charged residues; red: negatively charged residues. (*D*) The N (red) to S (blue) mutation at position 520 changes hydrogen bonding (yellow dashes) between the β-strands of the preceding blade of the WD40 β-propeller domain. (*E*) Substitution of Y residues 563, 603, and 621 (red) with charged and polar (blue) residues results in loss of hydrophobic interaction (purple – light pink dashes). (*F*) The W (red) to R (blue) substitution at position 400 abrogates hydrophobic interactions with several residues involving multiple β-propeller units. (*G*) WT and meningioma-associated mutant forms of TRAF7 can form homo- and hetero-dimers. (*H*) Mutant TRAF7 disrupts the interaction with endogenous MEKK3. Coimmunoprecipitation analysis in HEK293 cells. (*I*) Low concentrations of mutant TRAF7 (C388Y) are sufficient to disrupt the interaction of WT TRAF7 with MEKK3. Plasmids expressing C388Y (1, 2, 3, or 4 μg) and WT (4 μg) TRAF7 were cotransfected in HEK293 cells followed by immunoprecipitation for WT-TRAF7. (*J* and *K*) TRAF7 mutants display reduced ubiquitination in the absence (*J*) or presence (*K*) of exogenous MEKK3. (*L*) Surgically resected *TRAF7*-mutant meningiomas highly express TRAF7 (genotypes of tumors shown: MUN290: NF2; Yale 132: SMO W535L; MUN105: TRAF7 R641C/AKT1 E49K; MUN201: TRAF7 L580del/AKT1 E49K; Yale 25: TRAF7 G536S/KLF4 K409Q; MUN191: TRAF7 K615E/KLF4 K409Q). (Scale bar, 50 μm.) Confocal images captured under identical settings.

heterodimers (Fig. 1*G*), potentially explaining the impact of somatic heterozygous variants. TRAF7 interacts with MEKK3 and thus serves as a bona fide effector of the JNK and NF-kB pathways (2, 3, 17). All the four mutations diminished interactions of TRAF7 with MEKK3, albeit to different levels, depending on location (Fig. 1*H*). In addition, WT-mutant heterodimers displayed weaker interaction with MEKK3, suggesting that the mutants have dominant effects (Fig. 1*I*) and can disrupt WT protein function even at low levels of expression. As a result of the loss of interaction with MEKK3, TRAF7 mutants displayed reduced MEKK3-dependent ubiquitination (Fig. 1 *J* and *K*), abrogated JNK phosphorylation, and signaling (*SI Appendix*, Fig. S1 *D*–*G*). Consistent with these observations, surgically resected TRAF7-mutated meningiomas highly express TRAF7 protein, suggesting increased stability due to reduced auto-ubiquitination (Fig. 1*L*).

TRAF7 Mutations Are Associated with CHD. Based on this dominant effect of somatic TRAF7 mutations and motivated by a recent report of de novo missense variants in *TRAF7* in individuals with developmental delay and congenital anomalies, including heart defects (13), we interrogated our CHD cohort (18) comprising 2,645 parent–offspring trios and 226 singletons recruited to the Pediatric Cardiac Genomics Consortium (PCGC) and the Pediatric

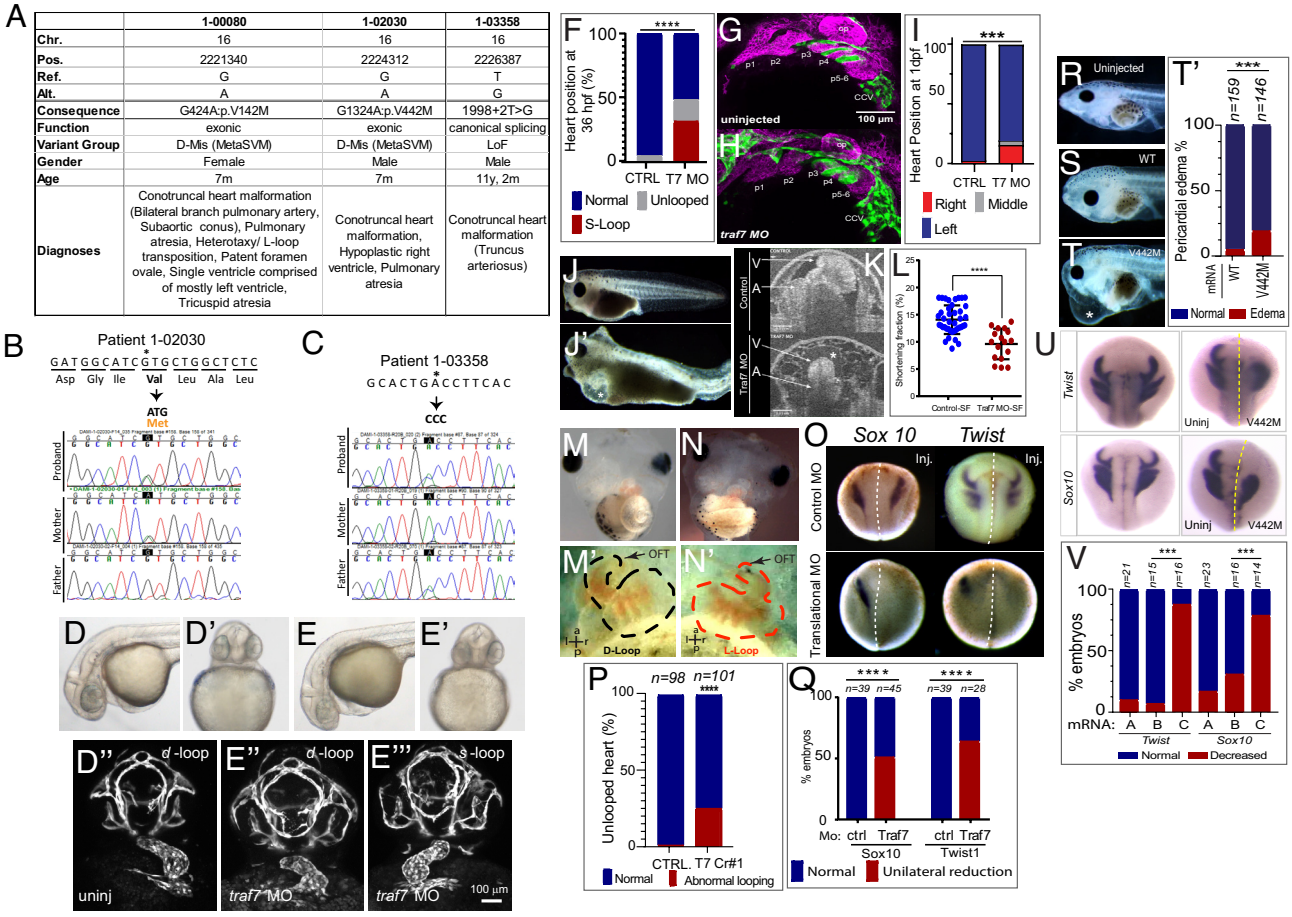

Fig. 2. TRAF7 mutations cause congenital heart defects: reduction of TRAF7 in zebrafish (*D*–*H*) and *Xenopus tropicalis* (*I*–*P*) as well as overexpression of mutant TRAF7 in *X. tropicalis* causes developmental defects (*Q*–*U*). (*A*) Clinical manifestations of patients harboring inherited *TRAF7* heterozygous developmental mutations. (*B* and *C*). Sanger sequencing traces of patients 1-02030 and 1-03358 and their clinically unaffected parents. The mutations are indicated in bold, and asterisk marks the mutated residue. (*D*–*F*) Injection of control (*D*–*D''*) or splice-site (*E*–*E'''*) TRAF7 MO in *tg(kdrl:GFP;gata-1:dsRed)* embryos results in pronounced heart looping defects at 36 hpf. (*F*). Quantification of embryos displaying cardiac looping defect ****: $P < 0.0001$ (Fisher's exact test; n= # of embryos). (*G* and *H*). Traf7 morphants exhibit reduced sox10 expression, disorganized pharyngeal arches. (*H*) Uninjected zebrafish (Tg:kdr:GFP, sox10:mRFP) embryo at 30 hpf showing pharyngeal arches 1 to 6 (p1 to p6). The otic placode (op) and common cardinal vein (CCV) are also labeled. (*I*) *TRAF7* morphant at the same stage. Note the reduced size of the pharyngeal arches, disorganization of p3 to p6, and reduced Sox10 expression. Green channel: endothelial cells; magenta: Sox10-expressing cells. (*I*) Distribution of heart position in control and TRAF7 1-d postfertilization morphants. Control: Left = 97.29% ± 3.29; middle= 0.83% ± 1.67; right= 1.88 ± 2.19, from 112 embryos total. TRAF7: *Left* = 76.31% ± 9.32; *Middle* = 3.07% ± 5.10; *Right* = 20.62 ± 9.99, from 112 embryos total. Two-way ANOVA with Bonferroni's multiple-comparison test, $P = 0.0004$ for left heart position. *J*–*K*. Injection of control (*J*) or splice-site (*J'*) TRAF7 MO in one-cell stage *Xenopus* embryos results in extensive pericardial edema (asterisk). Optical coherence tomography (OCT) highlights the edema (asterisk) and malformed heart (*K*), reflected in a significant reduction of the shortening fraction (*L*) at 3 dpf (stage 46) (Movie S3). Mann–Whitney test (scatter plot mean ± SD; n = 17, TRAF7 splice-site MO injected; n = 41, control MO injected.) *M*–*N'* TRAF7 CRISPR (CR#1) injection in one-cell stage *Xenopus* embryos results in pronounced heart looping defects at 48 hpf (*N*, *N'*) as compared to controls (*M*, *M'*) (Movie S4). OFT: outflow tract, V: ventricle. O. In situ hybridization analysis of *Xenopus* embryos (stage 16 to 18, 15 hpf): Unilateral injection (Inj.) with splice-site TRAF7, MO at two-cell stage shows disrupted expression of neural crest markers *Sox10* and *Twist* on the injected side when compared to the internal uninjected control. (*P*) Quantification of embryos displaying cardiac looping ****: $P < 0.0001$ (Fisher's exact test; n= # of embryos). (*Q*) Quantification of control or TRAF7 splice-site MO-injected embryos analyzed for *Sox10* and *Twist* expression. n = number of embryos. ****: $P < 0.0001$ (Fisher's exact test; n = # of embryos). (*R*–*T'*) Severe pericardial edema in *Xenopus* embryos following injection of *TRAF7* mRNA encoding mutant form V442M (*T*) but not WT (*S*) as compared to uninjected embryos (*R*). Quantification of embryos displaying pericardial edema (*T'*), ***: $P < 0.001$ (Fisher's exact test, n = # of embryos). (*U*) In situ hybridization analysis of *Xenopus* embryos (stage 17, 18 hpf): Decreased expression of the neural crest markers Twist and Sox10 following unilateral injection of TRAF7 V442M mRNA at the 2-cell-stage. (*V*). Quantification of control or TRAF7 splice-site MO-injected embryos analyzed for *Sox10* and *Twist* expression. *A* = Control, *B* = WT TRAF7, *C* = V442M TRAF7. ***:*P < 0.001:* Pairwise Fisher's exact test with FDR correction, n = # of embryos.

Heart Network (PHN) programs. We identified rare inherited ("developmental") mutations in *TRAF7* in three individuals (1-00080, 1-02030, and 1-03358) with CHD (Fig. 2*A* and *SI Appendix*, Fig. S2 *A* and *B* and Tables S1 and S2 and Dataset S1), who do not have any known trisomies or CHD-associated CNVs. The unaffected parents also harbored the alterations, indicating incomplete penetrance (Fig. 2 *B* and *C* and *SI Appendix*, Fig S2 *B* and *C*). All three patients presented with conotruncal heart defects of varying severity (Data Table 3): patient 1-00080 presented with tricuspid atresia and HTX (heterotaxy/L-transposition); patient 1-02030 displayed hypoplastic right ventricle and pulmonary atresia, whereas patient 1-03358 displayed truncus arteriosus. All three also arose from complex family structures and although they had normal facial features, one had right-hand oligodactyly, and another had polycystic kidney disease (Data Table 3). Segregation of variants was confirmed by Sanger sequencing or by assessing the BAM files (Fig. 2 *B* and *C* and *SI Appendix*, Fig. S2*A*). Missense mutations p.V142M (patient 1-00080) and p.V442M (1-02030) map to highly conserved residues (*SI Appendix*, Fig. S2*B*) and are predicted to be deleterious in MetaSVM, whereas the canonical splice-site variant 1998+2T>G (1-03358) is predicted to disrupt splicing between exons 20 and 21. None were identified in the Exome Aggregation Consortium (ExAC) database (19).

Structural protein modeling suggested that of the three inherited developmental mutations, p.V142M, which localizes to the RING domain, potentially impacts auto-ubiquitination, while p.V442M and 1998+2T>G are predicted to disrupt β-propeller structure; the former would affect the WD40 domains, and hence dimerization, whereas the latter would alter splicing, thus disrupting the last β-sheet. Therefore, based on modeling, both the developmental and the meningioma-associated heterozygous mutations would be expected to phenocopy loss of TRAF7 function. At the very least, 1998+2T>G is, indeed, a loss-of-function variant, and *TRAF7* has a missense Z score of 3.34 in ExAC, suggesting haploinsufficiency and extreme intolerance to missense mutations.

To gain insight into the association of *TRAF7* alterations with both meningioma and CHD, we investigated its expression profile. In the developing mouse embryo, *Traf7* mRNA is highly enriched in the neural tube as early as embryonic day (E) 8.5 and overlaps with the neural crest marker *Sox10* (*SI Appendix*, Fig. S3 *A–D'*). At E10.5, *Traf7* is expressed in the heart (*SI Appendix*, Fig. S3*E*) as well as in the trigeminal and geniculate ganglia, and in the first and second branchial arches, along the path of neural crest cell migration (*SI Appendix*, Fig. S3 *C–D'*). *Traf7* is highly expressed (90th percentile) in mouse meninges (*SI Appendix*, Fig. S3 *F–G'*), similar to *Akt1, Klf4, Polr2a, and Nf2* (above 90th percentile), all encoding established meningioma drivers (*SI Appendix*, Fig. S3*H* and Dataset S2).

Loss of TRAF7 Causes Cardiac Defects in Model Organisms. The association of inherited (this study) and de novo (13) *TRAF7* variants with CHD and craniofacial defects prompted us to test the effect of TRAF7 loss in vivo using *Xenopus* and zebrafish models. Splice-site morpholino-mediated knockdown of TRAF7 in zebrafish resulted in significant heart looping defects in 36 h post fertilization (hpf) morphant zebrafish embryos (Fig. 2 *D–F* and *SI Appendix*, Fig. S4*A*) as compared to controls with disorganized pharyngeal arches and reduced sox10 expression (Fig. 2 *H* and *I*). We also assessed for defects in heart jogging, a precursor for cardiac looping in zebrafish (20), and found a significantly higher incidence of abnormalities in the 26 hpf TRAF7 morphants as compared to the controls (Fig. 2*I*). We find an ensuing marked pericardial edema and (Fig. S4 *C–F* and Movies S1 and S2) significantly impaired heartbeat (*SI Appendix*, Fig. S4*G*) at 4 d post fertilization (dpf). We note that although the zebrafish heart consists of a single atrium and ventricle that do not septate, the genetic pathways and morphogenetic mechanisms underlying cardiac development in fish and mammals are strikingly similar (21, 22).

In *Xenopus,* TRAF7 morphants showed ventricular pump dysfunction, indicated by pericardial edema (Fig. 2 J and J'), and a significant reduction in the shortening fraction (23), measured by optical coherence tomography (OCT) (23, 24) (Fig. 2 *K* and *L* and Movie S3). TRAF7 reduction also resulted in abnormal cardiac looping (Fig. 2 *M–N'* and *P* and Movie S4), suggesting left–right patterning defects. Furthermore, TRAF7 knockdown by unilateral injection of morpholinos at the 2-cell stage disrupted the expression of neural crest markers *Sox10* and *Twist* on the injected side (Fig. 2 *O* and *Q*).

TRAF7 knockdown in *Xenopus* also resulted in craniofacial defects, including encephalocele/acrania (Fig. S5 *A–L'* and *M*). OCT analysis highlighted abnormalities in the formation of Meckel's, ceratohyal, and gill cartilages, disrupting the oral cavity (*SI Appendix*, Fig. S5 *N–P*). Similarly, morpholino-injected zebrafish also displayed craniofacial defects of varying severity, including an incorrectly angled hyoid arch, and an overall reduction in the size of Meckel's cartilage and the developing craniofacial skeleton at 7 dpf (*SI Appendix*, Fig. S5 *Q–R'*).

Finally, consistent with the dominant effects seen with meningioma-associated TRAF7 mutations (Fig. 1*I*), microinjection of mRNAs encoding the developmental mutant forms of TRAF7 (V442M and T601A) in one-cell stage *Xenopus* embryos resulted in significant pericardial edema (Fig. 2 *R–T'* and *SI Appendix*, Fig. S6*A*), craniofacial defects (*SI Appendix*, Fig. S6 *B–E*), and marked perturbation of neural crest cell markers (Fig. 2 *U* and *V* and *SI Appendix*, Fig S6 *F–H*). Taken together, these observations support the notion that the developmental mutations also have dominant effects, similar to the meningioma-associated variants.

TRAF7 Depletion Leads to Defective Ciliogenesis. In addition to heart looping defects, the TRAF7 knockdown *Xenopus* and zebrafish mutants also displayed the classic features of ciliopathy: curved body axis, hydrocephaly, and kidney cysts. Zebrafish morphants displayed substantial ventrally directed curling (Fig. 3 *A*, and *B–E*), kidney cysts appearing as small spherical clearings in the pronephros (Fig. 3 *A* and *B–F*), and intracranial fluid accumulation (Fig. 3 *C*, *D–G*). Similarly, in *Xenopus*, translational morpholino as well as CRISPR/CAS9 knockdown of TRAF7 resulted in curved body axis (Fig. 3 *H–L*) and cranial defects and hydrocephaly (Fig. 3 *H–K* and *M*). Notably, the abnormal cranial phenotype can be rescued by injecting WT TRAF7mRNA (Fig. 3*N* and *SI Appendix*, Fig. S5 *A* and *B*). OCT imaging of 5 dpf TRAF7 morphant embryos showed a distinct increase in the size of the pronephros (Fig. 3 *O–Q* and Movie S5), which harbored an accumulation of vesicular bodies as seen by TEM analysis, reminiscent of precystic kidneys (Fig. 3*R*).

To investigate whether the overlap in the pathobiology of meningioma harboring somatic mutations in *TRAF7* and neural crest cell pathologies including congenital cardiac and craniofacial defects might be due to defects in cilia-related/regulated processes, we focused on TRAF7 interactors. Using the single-cell transcriptomic data of the developing telencephalic and diencephalic meninges (25), we recapitulated the published results but added Markov Affinity-based Graph Imputation of Cells (MAGIC) (26), Potential of Heat-diffusion for Affinity-based Trajectory Embedding (PHATE) (27), and Density-Resampled Estimate of Mutual Information (DREMI) (28) analyses to infer gene–gene relationships (Fig. 3 *S* and *T*). The genes most commonly involved in meningioma (*Traf7*,

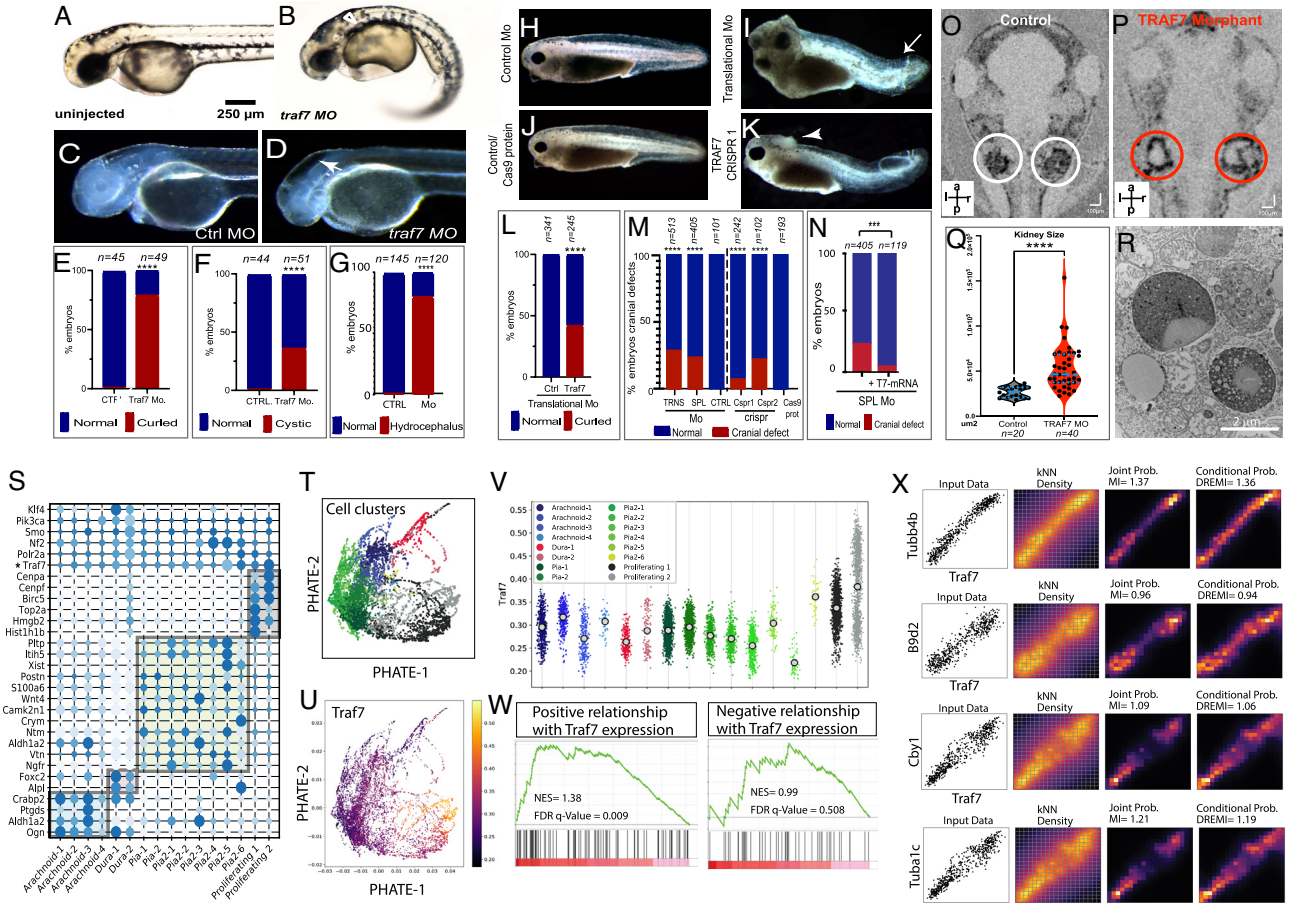

Fig. 3. Reduction of TRAF7 causes ciliopathy phenotypes in zebrafish (*A*–*G*) and *Xenopus tropicalis* (*H*–*R*), and single-cell transcriptomic analysis reveals TRAF7 association with cilia-related genes (*S*–*V*). (*A* and *B*) Pronephric cysts and axial curvature in 2.5 dpf Traf7 morphant zebrafish larva (*A*) but not control (*B*). Embryos exhibit substantial ventrally directed curling and cysts that appear as small spherical clearings in the pronephros (arrowhead). (*C* and *D*) Hydrocephalus in 2 dpf embryos following injection of TRAF7 splice-site (*R*), but not control (*Q*), MO at the 1-cell stage. Quantification of embryos presenting with hydrocephalus (*S*) ****: *P* < *0.0001* (two-sided Fisher's exact test, n= # of embryos). (*E*) Quantification of curled-down phenotype. This occurs in ~75% of MO-injected embryos, but never in controls. ****: *P* < *0.0001* (two-sided Fisher's exact test, n= # of embryos). (*F*) Quantification of cystic phenotype. This appears in ~33% of MO-injected embryos, but never in controls. ****: *P* < *0.0001* (two-sided Fisher's exact test, n= # of embryos). (*G*) Quantification of hydrocephalus phenotype. This appears ~75% of the time in injected fish, but never in uninjected controls. ****: *P* < *0.0001* (two-sided Fisher's exact test, n= # of embryos). (*H*–*N*) Hydrocephalus and cranial (arrowheads) and tail (arrows) defects in 2 dpf (stage 38-39) in *X. tropicalis* embryos injected with translational (*I*) but not control (*H*) MO, or with CRISPR/Cas9 targeting TRAF7 (*K*), but not Cas9 alone (*J*). Scale bar: 200 µm. (*L*) Quantification of curled tail phenotype. This appears in ~47% of MO-injected embryos, but never in controls. ****: *P* < *0.0001* (two-sided Fisher's exact test, n = # of embryos); (*M*) Quantification of hydrocephalus/cranial defect phenotype. This appears in embryos injected with translational morpholino (~30%) and splice-site morpholino (~25%), but never in embryos injected with control morpholino. CRISPR2 injections are more effective (~25%) than CRISPR 1 (~12%) as compared to CAS9 in eliciting cranial defect phenotype. ****: *P* < 0.0001 (two-sided Fisher's exact test, n= # of embryos); (*N*) Rescue of cranial defects upon coinjection of 100 pg of WT-TRAF7 mRNA and splice-site TRAF7-MO. n = number of embryos. ***: *P* < *0.001* (two-sided Fisher's exact test, n = # of embryos). (*O*–*R*) Traf7 morphant (*P*) but not control (*O*) *X. tropicalis* embryos exhibit enlarged kidneys at 5 dpf as visualized by OCT; (*Q*) Quantification of kidney size: TRAF7 morphant embryos show a variable but overall significant increase in kidney size as compared to control embryos (Movie S5). ****: *P* < *0.0001* (two-sided Fisher's exact test, n= # of embryos); (*R*) Transmission electron microscopic analysis of the developing pronephros at 5 dpf shows large vesicular bodies suggestive of precystic kidneys. (*S*–*X*) scRNAseq analysis of E14.5 mouse meninges obtained from publicly available data (25). Dot plot showing mean expression for marker genes for the arachnoid, dura, pia, and proliferating cell clusters. The size and color density of the dots represent fraction of cells expressing the gene in the groups and mean expression, respectively. Shaded rectangles indicate genes enriched in cell clusters. * Indicating the relative expression of Traf7 within cell clusters (*S*). PHATE plot showing different cell clusters in scRNAseq data in (*S*). Colors representing cell clusters [see panel *V*] (*T*). PHATE plot demonstrating Traf7 expression profile in mouse meningeal cell clusters (*U*). Jitter plot showing enrichment of Traf7 in proliferating meningeal cluster, more prominently in Proliferating-2 subcluster (*V*). Gene set enrichment analysis (GSEA) indicating the enrichment of cilia-related genes (obtained from CiliaCarta Database) within the genes that show positive (*Left*) or negative (*Right*) association with Traf7 expression in knn-DREMI analysis. Positively associated genes demonstrating significant enrichment for cilia-related genes, while negatively associated genes do not. NES: Normalized enrichment score (*W*). Representative DREVI plots for the cilia-related genes showing strong positive relationship with Traf7 expression in knn-DREMI analysis (*X*).

Nf2, *Klf4*, *Smo*, *Polr2a*, and *Akt*) were visualized using PHATE, and expression in each cluster was pictured with Jitter plots using scprep (26). Among them, only *TRAF7* is highly expressed in the proliferative clusters (Proliferating Clusters 1 & 2) (Fig. 3 *T*–*V*) and *TRAF7* was specifically enriched in the "Proliferating Cluster 2" whose marker genes include centrosomal genes *Cenpf* and *Cenpa*.

Ranked DREMI scores were generated for Traf7, and Density-Rescaled Visualization (DREVI) (29) plots were used to cluster gene–gene relationships. This list was then used to perform gene set enrichment analysis (GSEA) on positively and negatively associated genes, separately (Fig. 3 *W* and *X*). This analysis revealed a significant enrichment of cilia-related genes only in the gene set positively correlated with *TRAF7* (normalized enrichment score (NES) = 1.38, *P* = 0.009, versus NES = 0.99 and *P* = 0.51 for negatively correlated gene sets) (Fig. 3 *W* and *X*). These observations suggest that *TRAF7* positively regulates cilia-related processes (NES = 0.99, *P* = 0.50).

Despite their anatomical overlap in neural crest derived-meninges anterior to the foramen magnum (7, 30), *TRAF7*- and *SMO*-driven meningioma subtypes display different gene expression signatures, with a noted activation of HH signaling only in the latter (31). Given the association of TRAF7 with cilia-related genes (Fig. 3*V*),

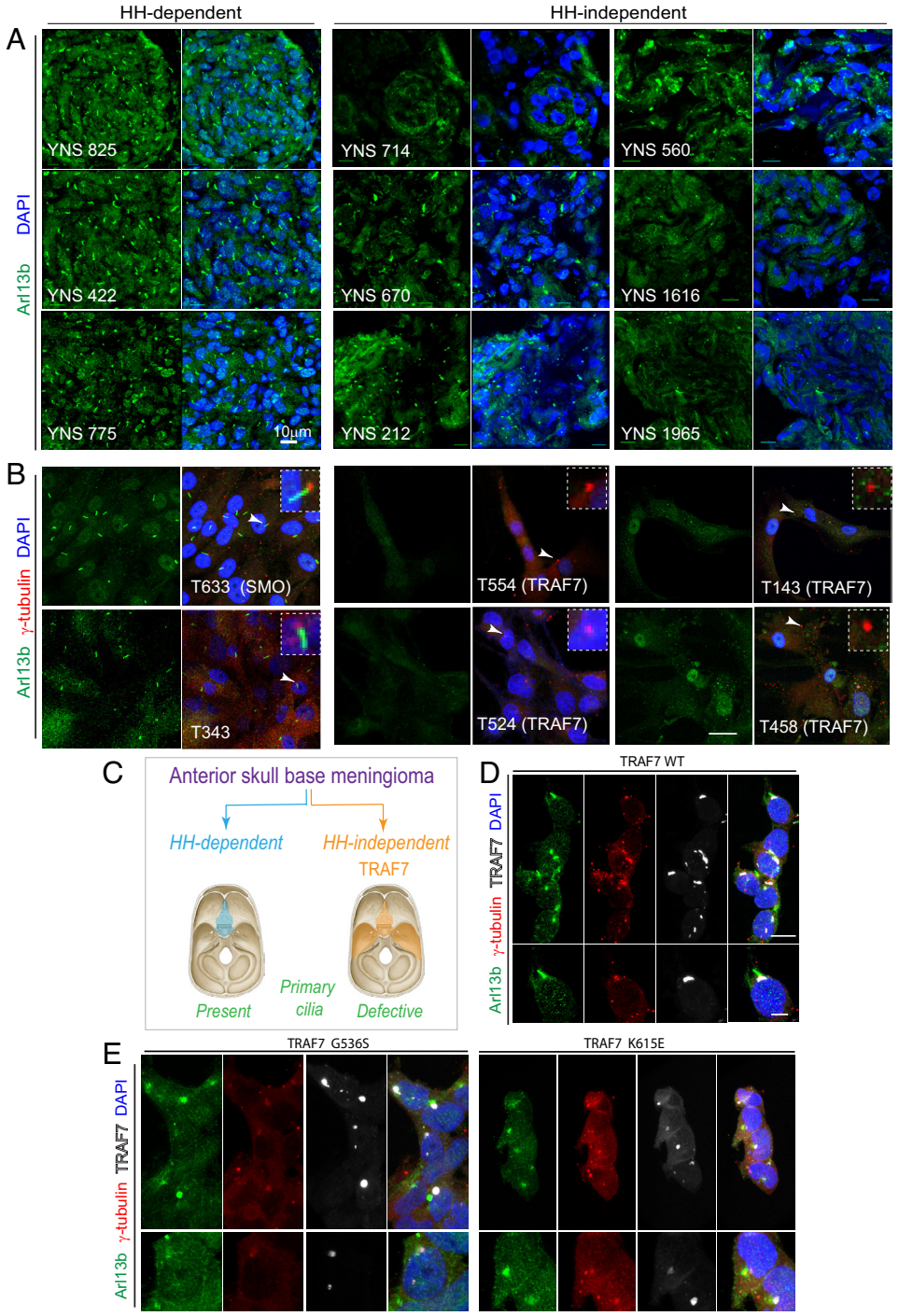

Fig. 4. Loss of primary cilia in TRAF7-driven meningiomas. (*A*) Meningiomas that are either HH-dependent or -independent [based on microarray analysis, (31)] stained for Arl13b (primary cilia) and DNA (DAPI). Confocal immunofluorescence microscopy reveals that HH-dependent tumors express primary cilia, while HH-independent (TRAF7 mutated) tumors display reduced, abrogated, or absence of primary cilia. Genotypes of tumors used YNS 825: SMO L412F; YNS 422 and YNS 775: HH-driven based on gene expression analysis, mutation unknown; YNS 714: TRAF7 unknown mutation/KLF4 K409Q; YNS 670: TRAF7 K498E/KLF4 K409Q; YNS 212: TRAF7 splice-site mutation: c.1135+5G>A/ AKT E17K; YNS 560: AKT1-E17K (± TRAF7); YNS 1616: TRAF7 I368N/KLF4 K409Q; YNS 1965: TRAF7: R653Q/AKT1-E17K. 3D projections of equivalent z-stacks are shown. (Scale bar, 10 μm.) (*B*) Primary cultures of meningiomas that are either HH-dependent or -independent [based on microarray analysis, (31)] stained for Arl13b (primary cilia) and γ-tubulin (centrosomes, marking base of cilia). Arrowheads indicate region shown at higher magnification in inset. All images captured under identical confocal settings. [Genotypes of cultures used T633 (derived from YNS 825): SMO L412F; T343 (derived from YNS 422) and T596 (derived from YNS 775): HH driven based on gene expression analysis, mutation unknown; T554 (derived from YNS 714): TRAF7 unknown mutation/KLF4 K409Q; T524 (derived from YNS 670): TRAF7 K498E/KLF4 K409Q; T143 (derived from YNS 212): TRAF7 splice-site mutation: c.1135+5G>A/ AKT E17K); T458 (derived from YNS 560): AKT1-E17K (±TRAF7). (Scale bar: 20 μm.) (*C*) Schematic representation of anatomic localization of HH-dependent (turquoise) and -independent (orange) meningiomas, driver mutations, and primary cilium status. (*D*–*E*) Overexpression of V5-tagged WT and mutant (G536S or K615E) TRAF7 in HEK293 cells followed by staining for Arl13b (green), γ-tubulin (red), and V5 (white, marking TRAF7). Only mutant forms of TRAF7 affect the primary cilium. (Scale bar: 20 μm.)

ciliopathy-related phenotypes in our model systems following TRAF7 depletion, and the dual involvement of the primary cilium in HH signaling as well as neural crest cell development (32, 33), we investigated whether *TRAF7* mutations impacted ciliogenesis. Immunostaining of tumors (Fig. 4*A*) and primary cultures (Fig. 4*A*') derived from surgically resected meningiomas for

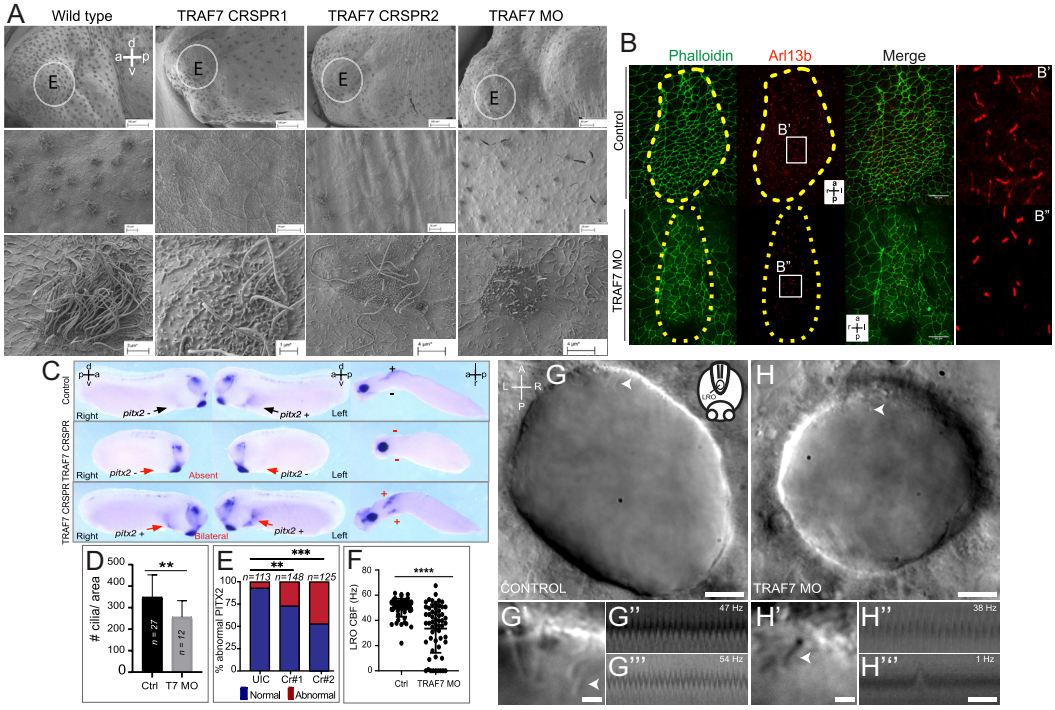

Fig. 5. TRAF7 knockdown in *Xenopus tropicalis* (*A–G*) and zebrafish (*H–J*″) affects mono- and multi-cilia in the left–right organizer (LRO). (*A*) Scanning electron microscopic images of *Xenopus* epidermis reveal defective cilia formation on TRAF7 depletion with either CRISPR #1, #2, or MO. Circled areas are magnified in the bottom panels. (Scale bars: Top row: 100 µm, middle row: 10 µm, bottom row: 3 µm.) (*B*) *Xenopus* embryos were injected at 1-cell stage and dorsal explants were prepared at stage 17 to visualize the left–right organizer (LRO). Specimens were processed for immunohistochemistry (IHC) to assess ciliation rate and cell surface area. Compared to uninjected controls, TRAF7 morphants have fewer cilia, as shown by acetylated tubulin (red) and phalloidin (actin, to outline cell boundaries; green). a = anterior, l = left, p = posterior, r = right. C. Analysis of *pitx2c* expression in stage 28 to 30 *Xenopus* embryos. Embryos are viewed laterally from the right (first column), the left (second column), and ventrally (third column). Expression of *pitx2c* is normally in the left lateral plate mesoderm (LPM, black arrow). CRISPR-mediated TRAF7 knockdown results in abnormal absent *pitx2c* expression with no *pitx2c* mRNA found in the left or right LPM (*Middle* panel, red arrows); or abnormal bilateral *pitx2c* expression with *pitx2c* mRNA found in both left and right LPM (*Bottom* panel, red arrows). (*D*) Bar plot demonstrating quantification of ciliation in relation to cell surface area in the LRO of TRAF7 morphant and control *X. tropicalis* embryos in (*C*). **: $P < 0.00$: *t* test with Welch correction, n= # of embryos. E. Quantification of *pitx2c* expression in uninjected controls (UICs) and traf7-G0 mutants by sgRNA#1 and #2. Abnormal includes absent and bilateral *pitx2c* expression. Statistical calculations were performed using a Chi-square test comparing the number of affected embryos against the number of wild-type embryos. **$P < 0.01$, ***$P < 0.001$; n, number of analyzed tadpoles. (*F–H*). TRAF7 is required for proper motility of cilia in zebrafish LRO. (*F*) Quantification of the ciliary beating frequency (CBF) in control (60 cilia from eight embryos) and TRAF7 morphants (58 cilia from eight embryos). Mean control CBF= 50.5 Hz ± 7.14. Mean TRAF7 CBF = 33.47 ± 19.15. Two-sample *t* tests, $P = 6.5 \times 10{-}9$; mean ± SD. Representative images of the LRO cilia of a control MO-injected embryo (eight somite stage) (*G* and *G*′) and of a TRAF7 MO-injected embryo (six somite stage) (*H* and *H*′) (Movies S7 and S8). (Scale bars: G, H = 10 µm; G′, H′ = 2 µm.) White arrows indicate cilia. *G*′ and *H*′ are close-ups of the imaged regions in the anterior side of the LRO in *G* and *H* (Movies S9–S12). Representative kymographs of two individual "control" cilia (*G*″ and *G*‴) and of TRAF7 knockdown cilia (*H*″ and *H*‴). Kymograph total duration 500 ms. (Scale bar, 100 ms.)

Arl13b (primary cilia) demonstrated that, unlike HH-dependent meningiomas, *TRAF7*-driven tumors displayed reduced, abrogated, or complete absence of primary cilia (Fig. 4 *A*, *A*′, and *B*). Similarly, in *Xenopus* embryos, quantification of primary cilia in the area next to the cephalic fold (where *Twist* and *Sox10* are expressed) showed a significant reduction in the number of cilia at the TRAF7 MO-injected side (*SI Appendix*, Fig. S8*C*). Consistent with a dominant effect of the mutations, overexpression of mutant forms of TRAF7 in HEK293 and primary neural crest cells also resulted in shortened cilia (Fig. 4 *C* and *D* and *SI Appendix*, Fig. S6).

Next, we examined the effect of TRAF7 knockdown on cilia in vivo. Reduction of TRAF7 in *Xenopus* embryos resulted in significant abrogation of both primary and motile cilia (Fig. S8 *A–D* and Fig. 5*A*), which appeared short and sparse. Furthermore, the motility of epidermal cilia was severely abrogated (Movie S6). In mammalian, fish, and *Xenopus* embryos, a cilia-driven leftward flow of extracellular fluid is required to initiate the nodal cascade that determines the left–right axis leading to asymmetric development (34). In *Xenopus*, activation of nodal signaling leads to the activation of pitx2c in the left lateral plate mesoderm (LPM) (35, 36), which is crucial for the asymmetric formation of heart (37, 38). Given the CHDs associated with TRAf7 mutations, we analyzed motile monocilia in the left–right organizer (LRO) in *Xenopus* and Kupffer's vesicle (KV) in *zebrafish*. In *Xenopus* morphant stage 28 embryos, there was a marked reduction in the number of cilia in the LRO (Fig. 5 *B–B*″ and *D*). Furthermore, this reduction in cilia impacted the left-sided expression of *pitx2c*, which was either abnormally lost or bilateral in these TRAF7 knockdown embryos (Fig. 5 *C–E*). Similarly, in zebrafish TRAF7 morphant embryos, LRO cilia motility was significantly reduced or paralyzed (8 out of 58 analyzed cilia, Movies S8, S10, and S11), while cilia motility was normal in control embryos at the observed stages (Fig. 5 *F–H*″ and Movies S7 and S9). Some cilia with an erratic motility pattern were also observed in the TRAF7 morphants (Movie S12), while control embryos never displayed this behavior.

We found a similar impact on the ependymal monocilia and multicilia that are responsible for cerebrospinal fluid (CSF) movement in the central nervous system (CNS). In TRAF7 morphant embryos (*SI Appendix*, Fig. S9 *A–C*), the CSF velocity was severely impacted with a concomitant reduction in cilia in the telencephalon, diencephalon, and rhombencephalon (*SI Appendix*, Fig. S9 *D* and *E* and Movie S13).

TRAF7 Reduction Affects Cilia Motility and Intraflagellar Transport. To gain insight into the mechanism of how TRAF7 affects cilia, we assessed the known TRAF7 interactor, CYLD, a

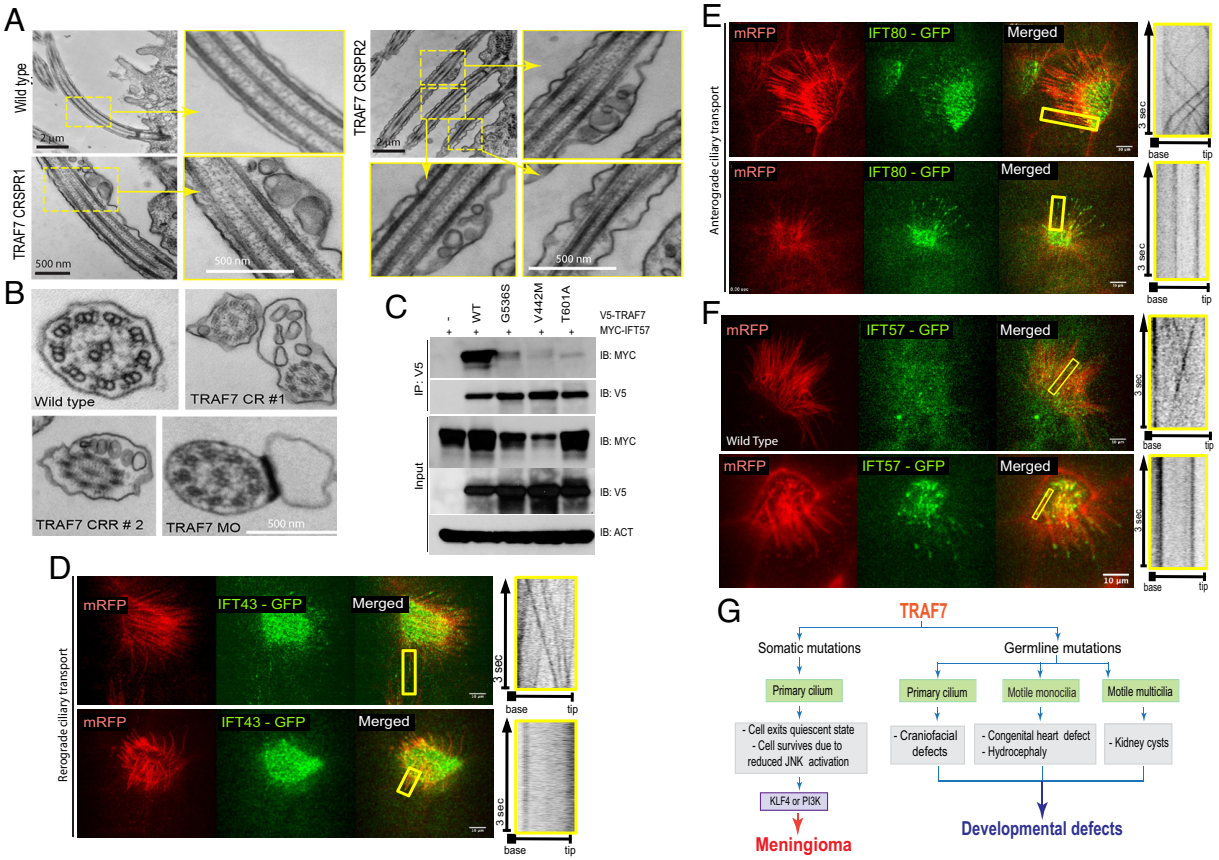

Fig. 6. TRAF7 interacts with IFT57, and its knockdown in *X. tropicalis* impairs intraflagellar transport. (*A* and *B*). TEM micrographs of cilia from the pronephros of WT- and TRAF7-morphant *Xenopus* embryos at 5 dpf. Low- and high (yellow boxes)-magnification views of flat-embedded sections of longitudinally sectioned cilia show frequent blebbing only in TRAF7 morphant samples. Cross-sections of cilia from WT and morphant embryos show the "9 + 2" microtubule doublet configuration with the presence of dynein arms. Sections of cilia in TRAF7 morphant embryos show frequent blebs containing electron-dense material. (*C* and *D*). In vivo imaging of IFT dynamics in *Xenopus* multiciliated cells. Still frames from a video of IFT43-GFP (*C*) and IFT80-GFP (*D*) to track intraflagellar transport in a multiciliated cell (Movies S14–16). Cilia are colabeled with mRFP. The yellow box indicates the cilia shown in the right kymograph, depicting still frames from a time-lapse video showing movement of a single control cilium. Time is indicated in seconds. (Scale bars, 10 µm.) (*E*) Meningioma and CHD- and craniofacial defect-associated TRAF7 mutants (G536S, V442M, and T601A, respectively) show reduced interaction with IFT57. Coimmunoprecipitation analysis in HEK293 cells. (*F*) In vivo imaging of IFT dynamics in *Xenopus* multiciliated cells. Still frames from a video of IFT57-GFP to track intraflagellar transport in a multiciliated cell (Movies S17 and S18). Cilia are colabeled with mRFP. The yellow box indicates the cilia shown in the right kymograph, depicting still frames from a time-lapse video showing movement of a single control cilium. Time is indicated in seconds. (Scale bars, 10 µm.) (*G*) *TRAF7* mutations disrupt ciliogenesis resulting in developmental (congenital heart and craniofacial) defects and disease (anterior skull-base meningioma).

multifunctional protein and an established mediator of ciliogenesis (39). Although mutant forms of TRAF7 lose interaction with CYLD (*SI Appendix*, Fig. S10 *A* and *B*), transmission electron microscopy (TEM) to examine the ultrastructure of cilia in the pronephros of *Xenopus* TRAF7 morphants showed frequent blebs containing electron-dense material (Fig. 6 *A* and *B*), a phenotype very different than the apical docking defects seen with CYLD loss (39). We then identified IFT57 (intraflagellar transport 57) protein, a component of the IFT B complex, as a potential binding partner of TRAF7. Intraflagellar transport is essential for cilia assembly and maintenance, and IFT57 displays a very significant probability of interaction (0.9999) with TRAF7 in BioPlex, a database of protein–protein interactions generated by affinity purification mass spectroscopy of human proteins (40, 41). We observed substantially diminished interactions of IFT57 with tumor- as well as CHD-associated TRAF7 mutants (Fig. 6*C*) upon overexpression in HEK293 cells.

IFT proteins form complexes incorporating anterograde kinesin motors or retrograde dynein motors to drive transport to the axonemal tip or the cell body, respectively. Hence, we examined the effect of TRAF7 knockdown on the movement of IFT proteins in *Xenopus* epidermal multicilia in vivo using swept field confocal microscopy followed by kymograph analysis. Fluorescently tagged anterograde (IFT80-GFP) or retrograde (IFT43-GFP) transport proteins were coinjected with membrane-tethered RFP (mRFP, to label the cilia) in the presence or absence of TRAF7 morpholino into one-cell stage *Xenopus* embryos. Both anterograde and retrograde transport were severely abrogated in the TRAF7 morphant embryos as compared to controls (Fig. 6 *D* and *E* and Movies S14–S16). Ciliary transport of IFT57-GFP was also severely retarded in TRAF7 morphant embryos (Fig. 6*F* and Movie S17 and S18).

Taken together, these observations support the hypothesis that TRAF7 plays a role in ciliary function and suggest that defective ciliogenesis may underlie both anterior skull-base meningiomas that are *TRAF7* driven and HH independent, as well as CHD associated with germline heterozygous *TRAF7* mutations (Fig. 6*G*).

Discussion

TRAF7 is considered to be a tumor suppressor (1, 42); more recently, it has also been attributed developmental functions (13). Although TRAF7 has been shown to regulate the MEKK3 and NF-κB pathways and to function as a scaffold for a variety of signaling molecules (1, 2, 17), the molecular underpinnings

of its action in tumorigenesis and development are not well understood.

In this study, we provide the mechanistic insight into TRAF7 mutant forms: They can heterodimerize with WT protein and disrupt its normal function, suggesting that they have dominant effects. We also report the cases of inherited, CHD-associated developmental *TRAF7* mutations, which are distinct from the numerous somatic variants we previously documented in meningioma (16). The developmental mutations are benign to the patients' unaffected parents, suggesting low penetrance, notwithstanding possible unreported mild phenotypes. Reduced penetrance is not uncommon; indeed, examples of bona fide disease-causing variants that fail to manifest in at least a proportion of carriers abound (43–45). The very limited number of available cases reported here prevents identification of any pattern that might determine incomplete penetrance, unlike, for example, *TP53* and *RB1*, where mutation type and location dictate penetrance (46, 47). Nevertheless, both the inherited developmental and the meningioma-associated somatic variants are heterozygous. Given our finding that mutant TRAF7 can interfere with WT function via heterodimerization and the haploinsufficiency of one of the developmental mutations (1998 + 2T > G), it is tempting to speculate that the variable phenotypes may reflect differential modulation of TRAF7 protein levels and/or function by the various mutant forms.

TRAF7 is highly expressed in neural crest and its derivatives, including the forebrain meninges, craniofacial skeleton, and heart outflow tract (*SI Appendix*, Fig. S3 *A–G'*), structures that are differentially affected in patients harboring *TRAF7* mutations leading to meningioma, craniofacial abnormalities, or CHD. In addition to TRAF7 mutated meningiomas arising from neural crest-derived meninges, we report several findings that support the role of TRAF7 in neural crest-derived structures. Specifically, *Traf7* is highly expressed in the developing mouse embryo and overlaps with the neural crest marker *Sox10* (*SI Appendix*, Fig S3 *A–D"*); in zebrafish, Traf7 morphants exhibit reduced *sox10* expression and disorganized pharyngeal arches (Fig. 2 *G* and *H*) – both of which are indicative of defective neural crest; in *Xenopus*, unilateral injection with TRAF7 MO at 2-cell stage disrupts expression of neural crest markers *Sox10* and *Twist* (Fig. 2 *O* and *Q*) with a concomitant reduction in primary cilia in the MO-injected half (*SI Appendix*, Fig. S8*C*); in *Xenopus* half injections, overexpression of TRAF7 V442M mRNA affects expression of the neural crest markers *Twist* and *Sox10* (Fig. 2 *U* and *V*), supporting the impact of mutant TRAF7 on neural crest; transfection of CHD-associated mutant TRAF7 (V442M, T601A), but not WT-TRAF7, into O9 primary neural crest cells abrogates primary cilia (*SI Appendix*, Fig. S7 *A–D*). Both, knockdown of TRAF7 and overexpression of TRAF7 mutant forms, result in craniofacial defects in *Xenopus* and zebrafish (*SI Appendix*, Figs. S5 *C–R'* and S6 *A–H*), supporting the neural crest impact of TRAF7 mutations; finally, in TRAF7 knockdown embryos, we also find clear evidence of hydrocephaly (*SI Appendix*, Fig. S10 *A–E*), which is associated with neural crest defects.

CHD and craniofacial abnormalities are characteristic of ciliopathies and led us to investigate the effect of TRAF7 loss on cilia. Importantly, meningioma-associated and developmental *TRAF7* variants disrupt interaction with IFT57, a component of the intraflagellar transport complex which is essential for the assembly and maintenance of flagella and cilia (48, 49). Cilia are devoid of protein synthetic machinery, and therefore all structural components, and any other protein cargo to be transported to or from the tip of the cilium, are dependent on IFT (50). IFT protein complexes containing anterograde and retrograde motors drive transport required for ciliary maintenance, which reflects the dynamic equilibrium between these ongoing antagonistic processes. IFT57 loss results in motility defects leading to abnormal flagellar beating. This is remarkably similar to our findings with TRAF7 loss which results in defective intraflagellar transport (Fig. 6 *D–E*), cilia motility defects (Movie S6), and ultimately degradation of cilia (Fig. 6 *A* and *B*).

In the realm of cancer biology, loss of primary cilium results in release from quiescent state of the cell cycle (51, 52). We have observed loss of primary cilium in TRAF7-driven skull-base meningiomas. We propose that in this context, TRAF7 mutations arise first and allow the cells to exit quiescence and survive by reducing JNK signaling (Fig. 6*G* and *SI Appendix*, Fig. S1) (17, 42, 53). A second PI3K or KLF4 mutation then allows the cell to proliferate and become tumorigenic. Markedly, among the skull base meningiomas, only primary cells derived from *TRAF7*-driven, but not *HH*-driven tumors, are devoid of primary cilia (Fig. 4), and the former display upregulation of Wnt, rather than HH, signaling (31), a finding underscored by the demonstrated reciprocal regulation between Wnt signaling and primary cilia (54). Together, these findings suggest that loss of cilia in *TRAF7*-driven meningiomas not only releases cells from quiescence but also relieves Wnt pathway regulation.

The primary cilium is also implicated in neural crest cell fate (33), and migrating neural crest cells bear primary cilia with which they sense morphogen gradients (55). Developmentally, the meninges surrounding the forebrain derive from neural crest, while those covering the rest of the brain and spinal cord originate from the somatic mesoderm (14, 56–58). TRAF7-driven meningiomas are located to the anterolateral skull base, which is covered by neural crest-derived meninges, supporting the neural crest origin of these tumors. The cephalic neural crest also contributes to the craniofacial skeleton (58), whereas the cardiac neural crest migrates to the heart and is essential for the septation of the cardiac outflow tract (59). Indeed, TRAF7 knockdown in both *Xenopus* and zebrafish leads to disruption of neural crest markers and primary cilia, and mainly impacts heart and craniofacial development, supporting the role of TRAF7 in neural crest cells and ciliogenesis. Further, the developmental defects we document in our patients, as well as those recently reported (13), are frequently encountered in ciliopathies (40, 41).

From a biological perspective, the effect of *TRAF7* heterozygosity is remarkable and adds a new chapter to the correlation between congenital heart disease and brain disorders (60, 61). The available data on the CHD families are limited, precluding us from assessing any occurrence of meningiomas. Although patients with CHD get cancer earlier and at a higher rate (62), it is unclear whether genetic variants play a role. Our study provides one such common genetic variant and warrants further detailed investigation into the rate of cancer occurrence in CHD families.

In summary, we demonstrate that somatic *TRAF7* mutations interfere with WT protein function, not only disrupting its interaction with MEKK3 as well as JNK signaling, but also impacting its interaction with IFT57 and abrogating cilia maintenance. Moreover, we find that primary cilia defects underlie *TRAF7*-driven meningiomas and CHD. Mechanistically, the specific role of TRAF7 in cilia formation involves IFT57 and, likely, additional interacting proteins, supporting the previously suggested link between ciliogenesis and tumorigenesis (52, 63). Finally, although *TRAF7* mutations can impact many different mechanisms, our studies suggest that loss of primary cilia in the neural crest and its derived structures may be a common theme underlying the ability to initiate both, tumorigenesis and developmental defects.

Materials and Methods

Plasmid Construction. V5- and Myc-tagged TRAF7 constructs were generated using the Gateway system.

Cell Culture and Meningioma Primary Cell Culture. HEK293 cells were maintained in DMEM supplemented with 10% FBS and penicillin/streptomycin. All tumor samples were deidentified prior to use, and IRB approval from Yale University, along with informed consent from all included study participants, was obtained. The tumor sample was washed in 1X RPMI, chopped into small pieces (<1 mm), and the fragments were digested with a mixture of collagenase type I and IV (0.5 mg/mL in PBS; Sigma-Aldrich, St. Louis, MO, USA) for 60 min at 37 °C. A single-cell suspension was prepared straining the cells through a 100-μm mesh cell strainer and spun at 1,000 g for 5 min. The cell pellet was resuspended in DMEM/F12 supplemented with 20% fetal bovine serum (Life Technologies), in a humidified atmosphere of 5% CO2/air. Cells were split at no more than 1:3 per passage and used up to passage 7.

Protein Work. Cell extracts were prepared in a Tris-based buffer containing 0.5% NP40 and used for immunoprecipitation with specific antibodies and Protein A+G DynaBeads (Life Technologies). Proteins were eluted with 1% SDS loading buffer and subjected to western blotting. Ubiquitination assays were performed as described previously (2). Briefly, cells were harvested in lysis buffer (2% SDS, 150 mM NaCl, 10 mMTris-HCl, pH 8.0) and boiled. Sonication was performed to shear the DNA. Lysates were diluted in dilution buffer (10 mM Tris-HCl, pH 8.0, 150 mM NaCl, 2 mM EDTA, 1% Triton) and incubated at 4 °C for 30 to 60 min. DynaBeads were incubated with appropriate antibodies and applied to the lysates. Samples were eluted with 1% SDS loading buffer and subjected to western blotting.

Animals. Mice were maintained in compliance with NIH guidelines and as approved by the Yale University Institutional Animal Care and Use Committee. *Xenopus tropicalis* and Zebrafish were maintained and cared for in our aquatics facility, in accordance with Yale University Institutional Animal Care and Use Committee protocols.

Morpholino oligonucleotides were ordered from Gene Tools, LLC
For *X.tropicalis*:
- Translational-MO (6-12ng/embryo; 5′-CGCGGGTTCTTATTTGAGGTCATAA-3′)
- Splice-MO (3-6ng/embryos; 5′-AGGATCATTCCTTACCCCGTTGCTG-3′)
- Standard control-MO (6 to 9ng/embryo 5′- CCTCTTACCTCAGTTACAATTTATA -3′)

sgRNA sequences are used for G0 (generation 0) injections:
-5′-GGTAACGGGCTTGCCATTGG-3′
-5′-GGGACACTTTTCTGCCGGAG-3′
-5′-GGCAGTTTGGCGTTATCCAC-3′
For *zebrafish*:
5′-CAGAAGATTGCTGACACTCACCGTG-3′ splice morpholino and
5′-ATCCATTTTGGCCTTGTTGGTGATG-3′) morpholino blocking translation
Supplementary Information includes detailed *SI Appendix, Materials and Methods*.

Data, Materials, and Software Availability. All study data are included in the article and/or *SI Appendix*.

ACKNOWLEDGMENTS. We would like to acknowledge the efforts and invaluable support of the operating room team at Yale New Haven Hospital in helping procure tumor samples for this study. We thank the Center for Cellular and Molecular Imaging, Electron Microscopy Facility at Yale Medical School, for assistance with the work presented here. This work was supported by the James Hudson Brown–Alexander Brown Coxe Postdoctoral Fellowship, an American Heart Association Postdoctoral Fellowship, and the National Heart, Lung, and Blood Institute of the NIH Award Number K99HL143036 (to S.C.J); NIH grant 1R01HL165241-01, Charles Hood Foundation and American Heart Association (to S.Y.); American Heart Association Postdoctoral Fellowship (to L.D.); NIH grant R21NS116484-02 and R01NS127879-01 (to E.D); Yale University funds, Gregory M. Kiez and Mehmet Kutman Foundation, and NIH grant 1R01NS110824-01A1 (for elucidating the molecular mechanism of TRAF7 in meningiomas only) (to M.G.)

Author affiliations: [a]Department of Neurosurgery, Yale School of Medicine, New Haven, CT 06510; [b]Department of Genetics, Yale School of Medicine, New Haven, CT 06510; [c]Cardiology Division, Department of Medicine, Cardiovascular Research Center, Massachusetts General Hospital and Harvard Medical School, Boston, MA 02129; [d]Department of Pediatrics, Yale School of Medicine, New Haven, CT 06510; [e]Department of Internal Medicine, Section of Cardiology, Yale Cardiovascular Research Center, Yale School of Medicine, New Haven, CT 06510; [f]Laboratory of Human Genetics and Genomics, The Rockefeller University, New York, NY 10065; [g]Yale Program in Brain Tumor Research, Yale School of Medicine, New Haven, CT 06510; and [h]Department of Neuroscience, Yale School of Medicine, New Haven, CT 06510

1. T. Zotti, I. Scudiero, P. Vito, R. Stilo, The emerging role of TRAF7 in tumor development. *J. Cell. Physiol.* **232**, 1233–1238 (2017).
2. T. Bouwmeester *et al.*, A physical and functional map of the human TNF-α/NF-κB signal transduction pathway. *Nat. Cell Biol.* **6**, 97–105 (2004).
3. L.-G. Xu, L.-Y. Li, H.-B. Shu, TRAF7 potentiates MEKK3-induced AP1 and CHOP activation and induces apoptosis. *J. Biol. Chem.* **279**, 17278–17282 (2004).
4. H. Yoshida, H. Jono, H. Kai, J. D. Li, The tumor suppressor cylindromatosis (CYLD) acts as a negative regulator for toll-like receptor 2 signaling via negative cross-talk with TRAF6 AND TRAF7. *J. Biol. Chem.* **280**, 41111–41121 (2005).
5. M. Tsikitis *et al.*, Traf7, a MyoD1 transcriptional target, regulates nuclear factor-kappaB activity during myogenesis. *EMBO Rep.* **11**, 969–976 (2010).
6. Q. T. Ostrom, G. Cioffi, K. Waite, C. Kruchko, J. S. Barnholtz-Sloan, CBTRUS statistical report: Primary brain and other central nervous system tumors diagnosed in the United States in 2014–2018. *Neuro. Oncol.* **23**, iii1–iii105 (2021).
7. V. E. Clark *et al.*, Genomic analysis of non-NF2 meningiomas reveals mutations in TRAF7, KLF4, AKT1, and SMO. *Science* **339**, 1077–1080 (2013).
8. D. E. Reuss *et al.*, Secretory meningiomas are defined by combined KLF4 K409Q and TRAF7 mutations. *Acta Neuropathol.* **125**, 351–358 (2013).
9. X. Liu *et al.*, Yamanaka factors critically regulate the developmental signaling network in mouse embryonic stem cells. *Cell Res.* **18**, 1177–1189 (2008).
10. R. Bueno *et al.*, Comprehensive genomic analysis of malignant pleural mesothelioma identifies recurrent mutations, gene fusions and splicing alterations. *Nat. Genet.* **48**, 407–416 (2016).
11. B. Goode *et al.*, Adenomatoid tumors of the male and female genital tract are defined by TRAF7 mutations that drive aberrant NF-kB pathway activation. *Mod. Pathol.* **31**, 660–673 (2017).
12. C. J. Klein *et al.*, Genomic analysis reveals frequent TRAF7 mutations in intraneural perineuriomas. *Ann. Neurol.* **81**, 316–321 (2017).
13. M. J. Tokita *et al.*, De Novo missense variants in TRAF7 cause developmental delay, congenital anomalies, and dysmorphic features. *Am. J. Hum. Genet.* **103**, 154–162 (2018).
14. J. A. Siegenthaler, S. J. Pleasure, We have got you 'covered': How the meninges control brain development. *Current Opinion Genet. Dev.* **21**, 249–255 (2011).
15. H. C. Etchevers, E. Dupin, N. M. Le Douarin, The diverse neural crest: From embryology to human pathology. *Development* **146** (2019).
16. M. W. Youngblood *et al.*, Correlations between genomic subgroup and clinical features in a cohort of more than 3000 meningiomas. *J. Neurosurg.* 1–10 (2019).
17. T. Zotti *et al.*, TRAF7 protein promotes Lys-29-linked polyubiquitination of IkappaB kinase (IKKgamma)/NF-kappaB essential modulator (NEMO) and p65/RelA protein and represses NF-kappaB activation. *J. Biol. Chem.* **286**, 22924–22933 (2011).
18. S. C. Jin *et al.*, Contribution of rare inherited and de novo variants in 2,871 congenital heart disease probands. *Nat. Genet.* **49**, 1593–1601 (2017).
19. M. Lek *et al.*, Analysis of protein-coding genetic variation in 60,706 humans. *Nature* **536**, 285–291 (2016).
20. D. T. Grimes *et al.*, Left-right asymmetric heart jogging increases the robustness of dextral heart looping in zebrafish. *Dev. Biol.* **459**, 79–86 (2020).
21. M. G. Grant, V. L. Patterson, D. T. Grimes, R. D. Burdine, Modeling syndromic congenital heart defects in zebrafish. *Curr. Top. Dev. Biol.* **124**, 1–40 (2017).
22. B. G. Bruneau, The developmental genetics of congenital heart disease. *Nature* **451**, 943–948 (2008).
23. E. Deniz *et al.*, Analysis of craniocardiac malformations in *Xenopus* using optical coherence tomography. *Sci. Rep.* **7**, 42506 (2017).
24. S. A. Boppart *et al.*, Noninvasive assessment of the developing *Xenopus* cardiovascular system using optical coherence tomography. *Proc. Natl. Acad. Sci. U.S.A.* **94**, 4256–4261 (1997).
25. J. DeSisto *et al.*, Single-cell transcriptomic analyses of the developing meninges reveal meningeal fibroblast diversity and function. *Dev. Cell* **54**, 43–59.e44 (2020).
26. D. van Dijk *et al.*, Recovering gene interactions from single-cell data using data diffusion. *Cell* **174**, 716–729.e727 (2018).
27. M. D. Luecken, F. J. Theis, Current best practices in single-cell RNA-seq analysis: A tutorial. *Mol. Syst. Biol.* **15**, e8746 (2019).
28. K. R. Moon *et al.*, Visualizing structure and transitions in high-dimensional biological data. *Nat. Biotechnol.* **37**, 1482–1492 (2019).
29. S. Krishnaswamy *et al.*, Systems biology. Conditional density-based analysis of T cell signaling in single-cell data. *Science* **346**, 1250689 (2014).
30. K. Dasgupta, J. Jeong, Developmental biology of the meninges. *Genesis* **57**, e23288 (2019).
31. V. E. Clark *et al.*, Recurrent somatic mutations in POLR2A define a distinct subset of meningiomas. *Nat. Genet.* **48**, 1253–1259 (2016).
32. S. C. Goetz, K. V. Anderson, The primary cilium: A signalling centre during vertebrate development. *Nat. Rev. Genet.* **11**, 331–344 (2010).
33. C. F. Chang, E. N. Schock, A. C. Attia, R. W. Stottmann, S. A. Brugmann, The ciliary baton: Orchestrating neural crest cell development. *Curr. Top. Dev. Biol.* **111**, 97–134 (2015).
34. A. G. Kramer-Zucker *et al.*, Cilia-driven fluid flow in the zebrafish pronephros, brain and Kupffer's vesicle is required for normal organogenesis. *Development* **132**, 1907–1921 (2005).

35. A. Kawasumi *et al.*, Left-right asymmetry in the level of active Nodal protein produced in the node is translated into left-right asymmetry in the lateral plate of mouse embryos. *Dev. Biol.* **353**, 321–330 (2011).
36. J. D. Lee, K. V. Anderson, Morphogenesis of the node and notochord: The cellular basis for the establishment and maintenance of left-right asymmetry in the mouse. *Dev. Dyn.* **237**, 3464–3476 (2008).
37. N. M. Davis *et al.*, The chirality of gut rotation derives from left-right asymmetric changes in the architecture of the dorsal mesentery. *Dev. cell* **15**, 134–145 (2008).
38. N. A. Kurpios, N. A. Sabolic, T. G. Shepherd, G. M. Fidalgo, J. A. Hassell, Function of PEA3 Ets transcription factors in mammary gland development and oncogenesis. *J. Mammary Gland. Biol. Neoplasia* **8**, 177–190 (2003).
39. T. Eguether *et al.*, The deubiquitinating enzyme CYLD controls apical docking of basal bodies in ciliated epithelial cells. *Nat. Commun.* **5**, 4585 (2014).
40. E. L. Huttlin *et al.*, Architecture of the human interactome defines protein communities and disease networks. *Nature* **545**, 505–509 (2017).
41. D. K. Schweppe, E. L. Huttlin, J. W. Harper, S. P. Gygi, BioPlex Display: An interactive suite for large-scale AP-MS protein-protein interaction data. *J. Proteome. Res.* **17**, 722–726 (2018).
42. I. Scudiero *et al.*, Tumor necrosis factor (TNF) receptor-associated factor 7 is required for TNFalpha-induced Jun NH2-terminal kinase activation and promotes cell death by regulating polyubiquitination and lysosomal degradation of c-FLIP protein. *J. Biol. Chem.* **287**, 6053–6061 (2012).
43. R. M. Shawky, Reduced penetrance in human inherited disease. *Egypt. J. Hum. Med. Genet.* **15**, 103–111 (2014).
44. J. Waalen, E. Beutler, Genetic screening for low-penetrance variants in protein-coding genes. *Annu. Rev. Genom. Hum. Genet.* **10**, 431–450 (2009).
45. D. N. Cooper, M. Krawczak, C. Polychronakos, C. Tyler-Smith, H. Kehrer-Sawatzki, Where genotype is not predictive of phenotype: towards an understanding of the molecular basis of reduced penetrance in human inherited disease. *Hum. Genet.* **132**, 1077–1130 (2013).
46. E. R. Kastenhuber, S. W. Lowe, Putting p53 in context. *Cell* **170**, 1062–1078 (2017).
47. J. Kamihara *et al.*, Retinoblastoma and neuroblastoma predisposition and surveillance. *Clin. Cancer Res.* **23**, e98–e106 (2017).
48. B. L. Krock, B. D. Perkins, The intraflagellar transport protein IFT57 is required for cilia maintenance and regulates IFT-particle-kinesin-II dissociation in vertebrate photoreceptors. *J. Cell Sci.* **121**, 1907–1915 (2008).
49. S. S. Siller, M. C. Burke, F. Q. Li, K. Takemaru, Chibby functions to preserve normal ciliary morphology through the regulation of intraflagellar transport in airway ciliated cells. *Cell Cycle* **14**, 3163–3172 (2015).
50. J. M. Scholey, Intraflagellar transport. *Annu. Rev. Cell Dev. Biol.* **19**, 423–443 (2003).
51. E. Peixoto, S. Richard, K. Pant, A. Biswas, S. A. Gradilone, The primary cilium: Its role as a tumor suppressor organelle. *Biochem. Pharmacol.* **175**, 113906 (2020).
52. H. Liu, A. A. Kiseleva, E. A. Golemis, Ciliary signalling in cancer. *Nat. Rev. Cancer* **18**, 511–524 (2018).
53. P. Najm *et al.*, Loss-of-function mutations in TRAF7 and KLF4 cooperatively activate RAS-like GTPase signaling and promote meningioma development. *Cancer Res.* **81**, 4218–4229 (2021).
54. J. B. Wallingford, B. Mitchell, Strange as it may seem: The many links between Wnt signaling, planar cell polarity, and cilia. *Genes. Dev.* **25**, 201–213 (2011).
55. J. De Calisto, C. Araya, L. Marchant, C. F. Riaz, R. Mayor, Essential role of non-canonical Wnt signalling in neural crest migration. *Development* **132**, 2587–2597 (2005).
56. G. F. Couly, P. M. Coltey, N. M. Le Douarin, The developmental fate of the cephalic mesoderm in quail-chick chimeras. *Development* **114**, 1–15 (1992).
57. K. M. Bagnall, S. J. Higgins, E. J. Sanders, The contribution made by cells from a single somite to tissues within a body segment and assessment of their integration with similar cells from adjacent segments. *Development* **107**, 931–943 (1989).
58. B. McBratney-Owen, S. Iseki, S. D. Bamforth, B. R. Olsen, G. M. Morriss-Kay, Development and tissue origins of the mammalian cranial base. *Dev. Biol.* **322**, 121–132 (2008).
59. M. L. Kirby, T. F. Gale, D. E. Stewart, Neural crest cells contribute to normal aorticopulmonary septation. *Science* **220**, 1059–1061 (1983).
60. J. Homsy *et al.*, De novo mutations in congenital heart disease with neurodevelopmental and other congenital anomalies. *Science* **350**, 1262–1266 (2015).
61. Y. H. Youn, Y. G. Han, Primary cilia in brain development and diseases. *Am. J. Pathol.* **188**, 11–22 (2018).
62. S. U. Morton *et al.*, Association of damaging variants in genes with increased cancer risk among patients with congenital heart disease. *JAMA Cardiol.* **6**, 457–462 (2021).
63. M. Higgins, I. Obaidi, T. McMorrow, Primary cilia and their role in cancer. *Oncol. Lett.* **17**, 3041–3047 (2019).